Received: 16 February 2021 | Revised: 22 April 2021 | Accepted: 6 May 2021

IET Microwaves, Antennas & Propagation

DOI: 10.1049/mia2.12158

The Institution of Engineering and Technology WILEY

ORIGINAL RESEARCH PAPER

Electromagnetic characterization of tuneable graphene-strips-on-substrate metasurface over entire THz range: Analytical regularization and natural-mode resonance interplay

Fedir O. Yevtushenko[1] | **Sergii V. Dukhopelnykov**[1,2] | **Tatiana L. Zinenko**[1] | **Yuriy G. Rapoport**[3]

[1]Laboratory of Micro and Nano Optics, Institute of Radio-Physics and Electronics NASU, Kharkiv, Ukraine

[2]Department of Applied Mathematics, V. N. Karazin, Kharkiv National University, Kharkiv, Ukraine

[3]Taras Shevchenko National University of Kyiv, Kyiv, Ukraine

Correspondence

Fedir O. Yevtushenko, Sergii V. Dukhopelnykov, Tatiana L. Zinenko, Laboratory of Micro and Nano Optics, Institute of Radio-Physics and Electronics NASU, 12, Ac. Proskura st.,Kharkiv, 61085, Ukraine.
Email: fedir.yevtushenko@gmail.com, dukh.sergey@gmail.com and tzinenko@yahoo.com

Yuriy G. Rapoport, Taras Shevchenko National University of Kyiv, 64/13, Volodymyrska Street, City of Kyiv, Kyiv, 01601, Ukraine.
Email: yuriy.rapoport@gmail.com

Funding information

the National Research Foundation of Ukraine, Grant/Award Number: 2020.02.0150

[Correction added on 18 June 2021, after first online publication, "DESIRED SAMPLING ERROR" was corrected to "DUAL SERIES EQUATION", on page 4, section 4 heading. Correction added on 29 July 2021, on page 6, equation 34, in the denominator, "m" was corrected to "±"]

Abstract

Scattering and absorption of the H-polarized plane wave by the infinite grating of flat graphene strips are considered in the environment met most frequently—on or at the surface of a dielectric-slab substrate. The full-wave meshless code is based on the analytical semi-inversion using the Riemann–Hilbert problem solution. This leads to a Fredholm second-kind matrix equation for the Floquet harmonic amplitudes that guarantees code convergence and provides easy control of computational error, which can be reduced to machine precision. The matrix elements are combinations of elementary functions, and therefore, the code is accurate and quite economical. This enables computation of the reflectance, transmittance, and absorbance as a function of the frequency in the wide band from static case to 10 THz. Numerical results show that such a metasurface with micrometre-sized strips is a composite periodic open resonator. It is highly frequency-selective thanks to the interplay of three types of natural modes—low-Q slab, moderate-Q plasmon strip, and ultra-high-Q lattice—that do not exist in the absence of the substrate. Varying the chemical potential of graphene, one can manipulate the electromagnetic characteristics of the metasurface at a fixed frequency from almost total transmission to almost total reflection.

1 | INTRODUCTION

Recent progress in nanotechnologies has drawn broad attention to graphene as a material that can provide new functionalities to devices and systems that use electromagnetic waves, especially in the terahertz, infrared, and visible-light ranges. This interest is explained by graphene's good conductivity, which can be tuned with the aid of DC electric biasing [1–4]. In addition, graphene can support a surface plasmon-guided wave with an electric field orthogonal to its surface in the terahertz and infrared ranges at frequencies two orders lower than those of the noble metals [5]. These properties make graphene very promising for designing novel tuneable antennas, filters, sensors, and absorbers, to mention just a few possible devices.

Today, the focus of research into the applications of graphene in electronics and photonics has shifted from wide-area sheets to patterned configurations in the form of strips, disks, and other flat forms [6]. One of the most intensively used configurations is a grating of parallel graphene strips [7–12]. In principle, graphene strips can be fabricated without substrate (suspended in air), thus improving their chemical stability [13].

_Patterned graphene configurations are typically located, however, on the surface of flat dielectric substrates. For instance, chemical vapour deposition (CVD) technology can produce a controlled number of high-quality graphene monolayers on a large area of high-refractive-index substrate. It was used in [10] to manufacture double-layer gratings of nanosize-width CVD-graphene strips on a substrate of polished float-zone silicon for infrared sensing. To pattern strips from the graphene sheet, 100-keV electron beam lithography and etching in oxygen plasma were applied.

Still, the technologies mentioned above are expensive. To reduce the cost and time of research and development, scientists have used the preceding modelling of the electromagnetic properties of patterned graphene. Of crucial importance here is the availability of the surface conductivity of non-patterned zero-thickness graphene in analytical form, known as the Drude model or the more sophisticated Kubo formalism [5]. Still, several aspects are non-trivial for accurate modelling and must fully account for Graphene's extremely thinness (1–2 nm) and finite and frequency-dependent conductivity as well as the presence of sharp edges, dielectric substrates, and superstrates. Comparative reviews of techniques employed for such modelling can be found in [14, 15] together with discussions of their limitations. In particular, it should be emphasized that the Fourier expansion technique (also known as 'rigorous coupled-wave analysis') is divergent in the H-polarization case [14], while commercial codes require the introduction of a nanoscale thickness of graphene that entails unnecessarily fine meshing and prohibitively long computation time [15]. Two analytical-numerical approaches stand out in this area: the method of singular integral equations (SIEs) solved using the Nystrom discretizations [16, 17] and the method of analytical regularization (MAR) applied to either SIE or other equivalent equations, casting them to Fredholm second-kind matrix equations [18–21].

The aim of our work is twofold. First, we would like to adapt the MAR version, which is based on the analytical solution of the Riemann–Hilbert problem (RHP) in complex calculus, to the analysis of wave scattering and absorption by an infinite grating of flat graphene strips lying on a flat dielectric-slab substrate. This MAR-RHP technique was developed earlier to analyze scattering from zero-thickness perfectly electrically conducting (PEC) on-substrate strip grating [22–24]. Its modification for graphene strips has not been done so far and is expected to outperform other techniques, including existing MAR-based techniques. The latter use SIEs in the spatial or Fourier-transform domain solved with the Galerkin method-of-moments with judiciously selected expansion functions (namely, weighted Chebyshev polynomials) [14, 21]. They are available only for graphene-strip gratings embedded in a layer of dielectric. In contrast, our MAR-RHP technique is equally applicable to embedded and on-surface configurations; it also has a great advantage in not needing numerical integrations to fill in the matrix equation.

Second, with the aid of such a trusted and efficient instrument, we aim to systematically research the resonance effects in the scattering and absorption of the terahertz waves by on-substrate graphene-strip gratings. Here, we focus our research on the so-called lattice-mode resonances, which do not exist on suspended graphene-strip gratings. They have been frequently overlooked or neglected earlier but became exposed recently [14, 21]. The lattice modes are specific natural modes of the gratings as periodic open resonators; they were first reported in [25] and then largely forgotten. However, they have attracted increasingly greater attention in recent times [19, 26–33]. This is because, in theory, they may have (for infinite gratings) various high-Q factors—for instance, if the substrate becomes thinner. The other natural modes of our composite scatterer, namely the plasmon modes of the strips and the slab modes of the substrate, do not have such a property. As noted in [14, 21], accurate quantification of such fine resonances appears to be possible only with the aid of truly sophisticated codes based on either MAR or SIE-Nystrom techniques.

In our work, we study only H-polarized plane wave scattering and absorption because in the case of E-polarization, plasmon-mode resonances do not exist. In the numerical experiments, we select the strip width, grating period, and substrate thickness in dozens of micrometres. This places the frequencies of the substrate, plasmon, and lattice modes in the terahertz range.

2 | PROBLEM FORMULATION

We consider an infinite flat grating of zero-thickness graphene strips, located in the plane $y = 0$ with period p, as shown in Figure 1. This plane is the upper surface of a homogeneous dielectric layer (substrate) of thickness h and relative dielectric permittivity ε. The graphene strips are assumed infinite along the z-axis and have the width d. The H-polarized plane wave is incident at the angle α with respect to the x-axis and depends on time as $e^{-i\omega t}$.

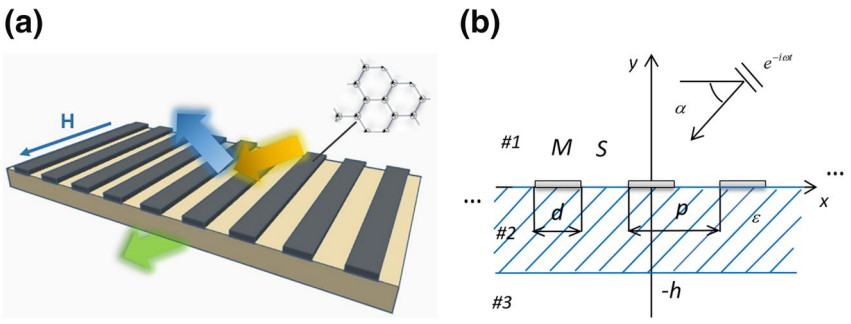

FIGURE 1 Infinite flat graphene-strip grating laying on a dielectric substrate and illuminated by a plane H-polarized wave (a) and cross-sectional geometry and notations used (b)

In the case of the H-polarization, the field components are $(E_x, E_y, 0)$ and $(0, 0, H_z)$. It is convenient to choose H_z as the 'basic' component; we denote it $U(x, y)$.

Then the incident field is a plane wave,

$$U^{in}(x,y) = e^{ik_0(\cos\alpha x - \sin\alpha y)}, y > 0, \tag{1}$$

where $k_0 = \omega/c = \omega(\varepsilon_0\mu_0)^{1/2}$ with c being light velocity. The entire field is decomposed into a sum, $U^{tot} = U^{in} + U^{(1)}$ in domain #1 and $U^{tot} = U^{(2,3)}$ in domains #2 and #3. Thus, we obtain the following boundary value problem for determining the function $U = U^{(j)}$, $j = 1, 2, 3$:

(I) it must satisfy the 2-D Helmholtz equation everywhere outside the strips and the slab interfaces:

$$\left(\nabla^2 + k_0^2\varepsilon^{(j)}\right)U^{(j)}(\vec{r}) = 0, \quad y \neq 0, y \neq -h, \ j = 1, 2, 3, \tag{2}$$

where we imply $\varepsilon^{(1)} = \varepsilon^{(3)} = 1$, $\varepsilon^{(2)} = \varepsilon$.

(II) resistive boundary conditions at the graphene strips on the upper interface, which is at $\vec{r} \in M : \{y = 0; |x + np| < d/2; \ n = 0, \pm1, \pm2, ...\}$, namely,

$$\frac{1}{ik_0}\frac{\partial}{\partial y}\left[U^{in}(x,y) + U^{(1)}(x,y) + \frac{1}{\varepsilon}U^{(2)}(x,y)\right]\Big|_{y=0} = -2Z\left[U^{in}(x,0) + U^{(1)}(x,0) - U^{(2)}(x,0)\right], \tag{3-a}$$

$$\frac{\partial}{\partial y}\left[U^{in}(x,y) + U^{(1)}(x,y) - \frac{1}{\varepsilon}U^{(2)}(x,y)\right]\Big|_{y=0} = 0, \tag{3-b}$$

and transparent boundary conditions at the slots, which are at $\vec{r} \in S : \{y = 0; -\infty < x < +\infty\}\backslash M$,

$$U^{(1)}(x,0) + U^{in}(x,0) = U^{(2)}(x,0), \tag{4-a}$$

$$\frac{\partial}{\partial y}\left[U^{in}(x,y) + U^{(1)}(x,y) - \frac{1}{\varepsilon}U^{(2)}(x,y)\right]\Big|_{y=0} = 0, \tag{4-b}$$

and similar conditions at the entire lower interface, $y = -h$, $-\infty < x < +\infty$,

$$U^{(2)}(x,-h) = U^{(3)}(x,-h), \tag{5-a}$$

$$\frac{\partial}{\partial y}\left[\frac{1}{\varepsilon}U^{(2)}(x,y) - U^{(3)}(x,y)\right]\Big|_{y=-h} = 0, \tag{5-b}$$

(III) the radiation condition, which means that at $y \to \pm\infty$, the scattered field must contain only the 'outgoing' waves, and

(IV) the condition of local finiteness of power: the power stored in any finite space domain D tends to zero if $D \to 0$; this condition determines the edge behaviour of the function U: it must tend to zero as a square root of the distance to the strip edges.

Conditions (I)–(IV) provide the uniqueness of the solution: if the function U exists, then it is unique. Additionally, the periodicity of the domain M, together with the shape of (1), entails the quasi-periodicity property,

$$U(x + p, y) = e^{-ik_0 p\cos\alpha}U(x,y), \tag{6}$$

which enables the reduction of the analysis to a single period of the scatterer.

3 | DUAL SERIES EQUATION

The quasi-periodicity property (6) allows expansion of the unknown field in terms of the Floquet series in each of the domains #1, #2, and #3. On introducing the dimensionless notations,

$$\begin{aligned} &\phi = 2\pi x/p, \quad \psi = 2\pi y/p, \quad \theta = \pi d/p, \\ &\xi = 2\pi h/p, \quad \kappa = p/\lambda, \end{aligned} \tag{7}$$

we can write these expansions as follows: in the upper half-space,

$$U^{(1)}(\phi,\psi) = \sum_{n=-\infty}^{+\infty} a_n e^{i(\gamma_n\psi + \beta_n\phi)}, \ \psi > 0, \tag{8}$$

in the dielectric substrate (domain #2),

$$U^{(2)}(\phi,\psi) = \sum_{n=-\infty}^{+\infty}\left(b_n e^{i\gamma_n^{sl}\psi} + c_n e^{-i\gamma_n^{sl}\psi}\right)e^{i\beta_n\phi}, \ 0 > \psi > -\xi, \tag{9}$$

and in the lower half-space (domain #3),

$$U^{(3)}(\phi,\psi) = \sum_{n=-\infty}^{+\infty} d_n e^{i(-\gamma_n\psi + \beta_n\phi)}, \ \psi < -\xi, \tag{10}$$

where unknown coefficients a_n, b_n, c_n, d_n are the amplitudes of the Floquet harmonics, and other notations are

$$\begin{aligned} &\gamma_n = \left(\kappa^2 - \beta_n^2\right)^{1/2}, \ \gamma_n^{sl} = \left(\kappa^2\varepsilon - \beta_n^2\right)^{1/2}, \ \beta_n = n - \beta_0, \\ &\gamma_0 = \kappa\sin\alpha, \quad \beta_0 = \kappa\cos\alpha, \end{aligned} \tag{11}$$

The reflectance and transmittance are the power fractions taken from the slab with grating to the upper and lower half-

space, respectively. They are expressed via the Floquet harmonic amplitudes as

$$P_{ref} = \gamma_0^{-1} \sum_{|n-\kappa\cos\beta|<\kappa} \gamma_n |a_n|^2,$$
$$P_{tr} = \gamma_0^{-1} \sum_{|n-\kappa\cos\beta|<\kappa} \gamma_n |d_n|^2. \quad (12)$$

The power absorbed in the metasurface can be found directly, as in [14, 21], or using the power conservation law,

$$P_{abs} = 1 - P_{ref} - P_{tr} \quad (13)$$

Substituting (9)–(10) into the conditions of (5), we obtain

$$\begin{cases} \sum_{n=-\infty}^{\infty} \left(b_n e^{-i\gamma_n^{sl}\xi} + c_n e^{i\gamma_n^{sl}\xi} \right) e^{i\beta_n\phi} = \sum_{n=-\infty}^{\infty} d_n e^{i\gamma_n\xi} e^{i\beta_n\phi} \\ \frac{1}{\varepsilon} \sum_{n=-\infty}^{\infty} \left(i\gamma_n^{sl} b_n e^{-i\gamma_n^{sl}\xi} - i\gamma_n^{sl} c_n e^{i\gamma_n^{sl}\xi} \right) e^{i\beta_n\phi} = \sum_{n=-\infty}^{\infty} -i\gamma_n d_n e^{i\gamma_n\xi} e^{i\beta_n\phi} \sum_{n=-\infty}^{\infty} -i\gamma_n d_n e^{i\gamma_n b + i\beta_n\phi} \end{cases} \quad (14)$$

Since these series coincide over the entire period, we replace them with termwise equations and express the unknowns b_n and c_n in terms of d_n:

$$b_n = \frac{1}{2} d_n e^{i\gamma_n\xi} \left(1 - \frac{\varepsilon}{\gamma_n^{sl}} \gamma_n \right) e^{i\gamma_n^{sl}\xi},$$
$$c_n = \frac{1}{2} d_n e^{i\gamma_n\xi} \left(1 + \frac{\varepsilon}{\gamma_n^{sl}} \gamma_n \right) e^{-i\gamma_n^{sl}\xi} \quad (15)$$

According to graphene conditions (3-a) and (3-b) at the strips, for $|\phi| < \theta$,

$$\frac{1}{\kappa} \left(-\kappa \sin\alpha e^{i\beta_0\phi} + \sum_{n=-\infty}^{\infty} a_n \gamma_n e^{i\beta_n\phi} + \frac{1}{\varepsilon} \sum_{n=-\infty}^{\infty} \left(\gamma_n^{sl} b_n - \gamma_n^{sl} c_n \right) e^{i\beta_n\phi} \right) = 2Z \left(\sum_{n=-\infty}^{\infty} \left(b_n + c_n \right) e^{i\beta_n\phi} - e^{i\beta_0\phi} - \sum_{n=-\infty}^{\infty} a_n e^{i\beta_n\phi} \right), \quad (16)$$

$$-\kappa \sin\alpha e^{i\beta_0\phi} + \sum_{n=-\infty}^{\infty} a_n \gamma_n e^{i\beta_n\phi} = \frac{1}{\varepsilon} \sum_{n=-\infty}^{\infty} \left(\gamma_n^{sl} b_n - \gamma_n^{sl} c_n \right) e^{i\beta_n\phi} \quad (17)$$

at the slots, $\vec{r} \in S$, conditions (4-a) and (4-b) yield, for $\theta < |\phi| < \pi$,

$$e^{i\beta_0\phi} + \sum_{n=-\infty}^{\infty} a_n e^{i\beta_n\phi} = \sum_{n=-\infty}^{\infty} \left(b_n + c_n \right) e^{i\beta_n\phi} \quad (18)$$

$$-\kappa \sin\alpha e^{i\beta_0\phi} + \sum_{n=-\infty}^{\infty} a_n \gamma_n e^{i\beta_n\phi} = \frac{1}{\varepsilon} \sum_{n=-\infty}^{\infty} \left(\gamma_n^{sl} b_n - \gamma_n^{sl} c_n \right) e^{i\beta_n\phi} \quad (19)$$

Thanks to (3-b) and (4-b), Equation (17) is satisfied over the entire period. Therefore, on substituting b_n and c_n from (15) and introducing new coefficients ($n = 0, \pm 1, \ldots$),

$$x_n = \left(-\delta_{n,0} \kappa \sin\alpha + \gamma_n a_n \right) (\Gamma_n)^{-1} + 2\delta_{n,0}, \quad (20)$$

$$\Gamma_n = \left[\frac{1}{\gamma_n} - \frac{\varepsilon}{\gamma_n^{sl}} \frac{\left(\gamma_n^{sl} - \gamma_n \varepsilon \right) e^{2i\gamma_n^{sl}\xi} + \left(\gamma_n^{sl} + \gamma_n \varepsilon \right)}{\left(\gamma_n^{sl} - \gamma_n \varepsilon \right) e^{2i\gamma_n^{sl}\xi} - \left(\gamma_n^{sl} + \gamma_n \varepsilon \right)} \right]^{-1}, \quad (21)$$

we arrive at the expression that links d_n and x_n:

$$d_n = \left(x_n - 2\delta_{n,0} \right) \Gamma_n \varepsilon e^{i\gamma_n\xi} \left[i\gamma_n^{sl} \sin\left(\gamma_n^{sl}\xi \right) + \gamma_n \varepsilon \cos\left(\gamma_n^{sl}\xi \right) \right]^{-1}. \quad (22)$$

Note that if $|n| \to \infty$, the weight function in (21) behaves as

$$\Gamma_n = \frac{i|n|}{1+\varepsilon} \left[1 + O\left(\frac{\kappa\cos\alpha}{|n|} \right) + O\left(\frac{\kappa^2}{n^2} \right) + O\left(e^{-|n|2\pi h/p} \right) \right] \quad (23)$$

4 | REGULARIZATION OF DUAL SERIES EQUATION

To achieve analytical regularization, we introduce the function

$$\Delta_n(\kappa, \varepsilon, h/p, \alpha, Z) = |n| + i(1+\varepsilon)\Gamma_n + i(1+\varepsilon)\kappa Z \quad (24)$$

and using the expressions (16)–(22), the following is the dual series equation (DSE) for the unknown coefficients, x_n:

$$\begin{cases} \sum_{n=-\infty}^{\infty} x_n |n| e^{in\phi} = \sum_{n=-\infty}^{\infty} x_n \Delta_n e^{in\phi} - i(1+\varepsilon) 2\Gamma_0, \theta < |\phi| \le \pi, \\ \sum_{n=-\infty}^{\infty} x_n e^{in\phi} = 0, |\phi| < \theta, \end{cases} \tag{25}$$

It can be verified that if all $\Delta_n = 0$, then (25) forms the RHP on an arc of the unit circle in the complex plane. This problem has an analytical solution expressed via the Plemelj–Sokhotski formulas, as explained, for instance, in [18, 22, 23]. Note that when building this solution, the edge condition (IV) is used explicitly. If this procedure is applied to the full DSE (25), it yields an infinite matrix equation,

$$x_m = \sum_{n=-\infty}^{\infty} A_{m\,n} x_n + B_m, m = 0, \pm 1, \pm 2, \ldots, \tag{26}$$

$$A_{m\,n} = \Delta_n T_{mn}(\theta), B_m = -i(1+\varepsilon) 2\Gamma_0 T_{m0}(\theta), \tag{27}$$

here, the functions $T_{mn}(\theta)$ are expressed via the Legendre polynomials P_m of the argument $u = -\cos\theta$ (see [18, 23]), namely,

$$T_{mn}(\theta) = \frac{(-1)^{m+n}}{2(m-n)} [P_m(u) P_{n-1}(u) - P_{m-1}(u) P_n(u)], m \ne n, \tag{28}$$

$$T_{00}(\theta) = -\ln\frac{1}{2}(1 + \cos\theta), \tag{29}$$

$$T_{mm}(\theta) = \frac{1}{2|m|} \left[1 + \sum\nolimits_{s=1}^{|m|} t_s(u) P_{s-1}(u) \right], m \ne 0, \tag{30}$$

where $t_0 = 1$, $t_1(u) = -u$, and $t_s(u) = P_s(u) - 2uP_{s-1}(u) + P_{s-2}(u)$.

The large-index asymptotics of the Legendre polynomials enable one to see that the following infinite sums are bounded:

$$\sum_{m,n=-\infty}^{+\infty} |A_{mn}|^2 < \infty, \sum_{m=-\infty}^{+\infty} |B_m|^2 < \infty \tag{31}$$

This is exactly what is needed to state that Equation (26) is a Fredholm second-kind matrix equation in the space of number sequences l_2. Hence, the convergence of its numerical solution for progressively larger truncation numbers N is mathematically guaranteed.

In [22], the inverted part of DSE was slightly different: namely, it involved the weight $|n| + const$ instead of $|n|$ in (25). This provided slightly faster convergence; however, it led to the Legendre functions of a complex-valued frequency-dependent index. In contrast, expressions (27) are combinations of elementary functions. In addition, they need no numerical integrations and hence can be easily computed with machine precision. This is an important advantage with respect to the other MAR-like techniques, such as MAR-Galerkin in the spatial or Fourier-transform domains [9, 12, 14, 19–21].

Inspection of (23), (24), and (27) shows that both Δ_n and $A_{m\,n}$ contain the terms proportional to the normalized frequency, $\kappa = p/\lambda$, and the terms proportional to $e^{-|n|2\pi h/p}$. This means that the regularization, which is the semi-inversion of DSE, is performed via the analytical inversion of the static limit of the part corresponding to the strip grating on the interface between two media, air and dielectric. As a result, both the existence of the finite substrate thickness and finite conductivity of strips must shift the 'threshold' value of the matrix truncation number, after which the error starts descending to larger values than in the case of suspended PEC strips: $N_{th} \approx \kappa[1 + h\varepsilon^{1/2}/p + (1+\varepsilon)|Z|]$.

5 | CONVERGENCE AND VALIDATION

To visualize the rate of convergence of the numerical solution, we compute the relative error, in the l_2-norm, of the solution found with varying truncation order N compared with $N = 400$ and defined as follows:

$$e_x(N) = \left(\sum_{n=-400}^{400} \left| x_n^N - x_n^{400} \right|^2 \right)^{1/2} \left(\sum_{n=-400}^{400} \left| x_n^{400} \right|^2 \right)^{-1/2} \tag{32}$$

The results in Figure 2a correspond to the normal and inclined incidence, $\alpha = 90^o$ and 45°, on the grating with $p = 70$ μm, $d = 14$ μm, $h = 10$ μm placed on the substrate with relative dielectric permittivity values $\varepsilon = 2.25$, 5, and 12; the frequency is 5 THz, which means $\kappa = 1.16$. The graphene parameters are $T = 300$K, $\mu_c = 0.39$ eV, and $\tau = 1$ ps, which results in the relative surface impedance $Z = 0.06 - i1.81$.

This value can be considered the near-field error. As shown in Figure 2a, it begins nearly exponential decay as soon as N becomes larger than $N_{th} \approx 20 - 30$, as explained in the previous section. In the analysis of plane wave scattering from gratings, normally the phenomena of reflection, transmission, and absorption in terms of power fractions are of primary interest. Therefore, we define and compute the far-field error as a function of N,

$$e_P(N) = |P_N - P_{400}|/P_{400}, \tag{33}$$

where P is transmittance, reflectance, or absorbance; see (12).

As seen in Figure 2b, with an increase in N over N_{th}, the error (33) starts decreasing similarly to near-field error; however, the value of that error is one to two orders smaller than for (32). As shown, the rate of convergence is the highest in the case of absence of the dielectric layer and normal incidence, while thinner and optically denser slabs entail larger values of

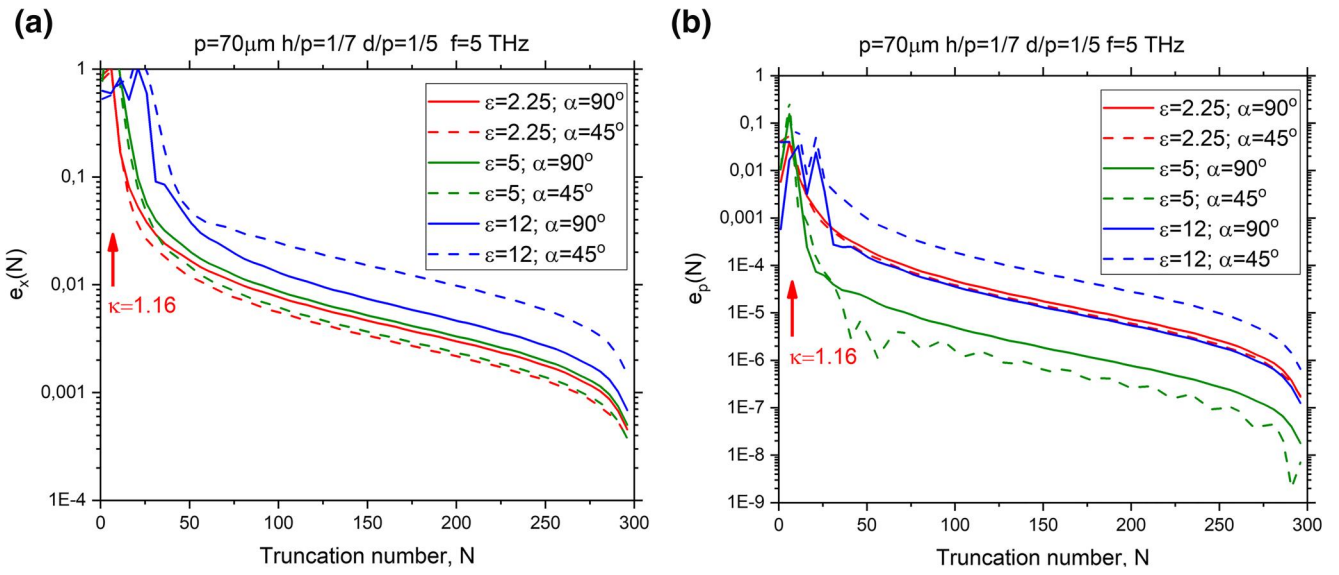

FIGURE 2 (a) The error in the computation of the Floquet harmonic amplitudes using (26)–(30) versus the matrix truncation order for the grating with parameters indicated in the inset. (b) The error in the computation of the reflectance. The frequency is $f = 5$ THz , and the graphene impedance is $Z = 0.06 - i1.81$

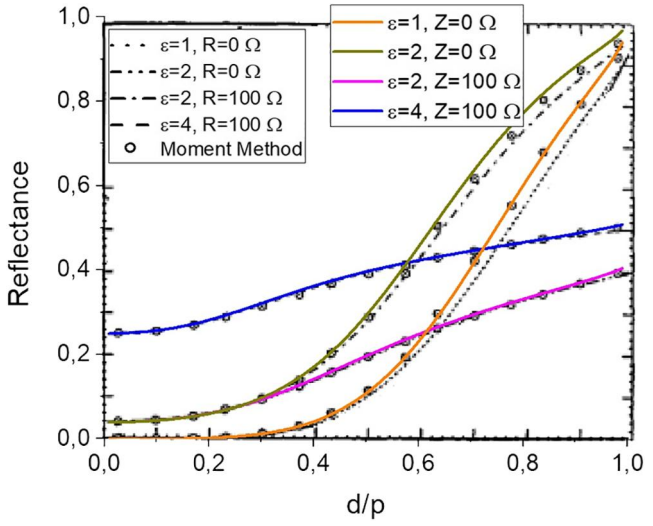

FIGURE 3 Comparison of the results of figure. 3a of [34] and MAR-RHP using (26)–(30). Reflectance of resistive-strip grating with $Z = 100$ Ohm on dielectric substrate versus the ratio d/p at $\kappa = 0.5$, $h/p = 0.2$, and $\varepsilon = 2$ and 4. The plots for the PEC strip array in the free space and on the same substrate are also shown

N to achieve the same accuracy. In contrast, the filling factor, d/p, does not change N_{th} or the rate of convergence.

Finally, as proof of validation, in Figure 3 we present a comparison of our results with those in fig. 3a of [34], computed by a conventional MoM code and a MAR-Galerkin with only one weighted Chebyshev polynomial approximating the strip current. Here, the absolute value of the zeroth-order Floquet harmonic is shown versus the filling factor, d/p, at the normalized frequency $\kappa = 0.5$ for resistive-strip grating with $Z = 100$ Ohm on dielectric substrate with $\varepsilon = 2$ and 4 and $h = p/5$ illuminated by the H-polarized plane wave incident at $\alpha = 60^o$. The PEC-strip case ($Z = 0$) is also shown for comparison. The corresponding curves visually overlap; the small discrepancy from MAR-Galerkin is explained by the low order of the latter and vanishes if $d/p \leq 0.3$.

6 | RAYLEIGH ANOMALIES AND NATURAL MODES

6.1 | Rayleigh anomalies

Rayleigh anomalies (RAs) are associated with the branch points of the field U as a function of the frequency at $\gamma_m = 0$; the existence of these branch points is the consequence of our assumption that the grating is infinite and the use of the Floquet series (8) and (10). Note that the frequencies at which $\gamma_m^{sl} = 0$ are not the branch points. Thus, in terms of the frequency $f = \omega/2\pi$, RAs are given by the following equations:

$$f_{\pm m}^{RA} = \frac{cmp^{-1}}{1 \pm \cos\alpha}, m = 1, 2, \ldots \tag{34}$$

If all periods of the grating are in the same phase, as at the normal incidence, the $\pm m$-th RA frequencies coalesce and correspond to the period being divisible by the free-space wavelength,

$$f_{\pm m}^{RA} = cm/p, m = 1, 2, \ldots \tag{35}$$

Note that the RA frequencies do not depend on the fine structure of the period of the grating.

6.2 | Substrate modes

In the absence of strips, the dielectric-slab substrate is the simplest 1-D open resonator, sometimes called the 'Fabry–Perot etalon'. Its natural modes S_m have complex-valued frequencies that are asymptotically given by the expressions found, for instance, in [35],

$$f_m^S \approx cm \Big/ \left(h\varepsilon^{1/2}\right), m = 1, 2, \ldots \tag{36}$$

The Q-factors of the slab modes are low, $Q_m^S \approx 10$. If the substrate is equipped with strips, the slab-mode frequencies shift in the complex plane; however, they do not disappear.

6.3 | Plasmon modes of the strips

As mentioned in the introduction, in the H-polarization regime, the grating of graphene strips demonstrates the resonances associated with the plasmon modes of each strip, P_m. Graphene's surface impedance is the sum

$$Z(\omega, \mu_c, \tau, T)Z_0 = 1/(\sigma_{\text{intra}} + \sigma_{\text{inter}}), \tag{37}$$

where σ_{intra} and σ_{inter} are the intraband (also known as the Drude term) and interband parts of the surface conductivity, respectively [5]. They are found from the Kubo formalism as

$$\sigma_{\text{intra}} = \frac{C}{\omega + i\tau^{-1}}, C = \frac{iq_e^2 k_B T}{\pi\hbar^2}\left[\frac{\mu_c}{k_B T} + 2\ln\left(1 + e^{-\frac{\mu_c}{k_B T}}\right)\right], \tag{38}$$

$$\sigma_{\text{inter}} = \frac{iq_e^2}{4\pi\hbar}\ln\frac{2|\mu_c| - (\omega + i\tau^{-1})\hbar}{2|\mu_c| + (\omega + i\tau^{-1})\hbar}, \tag{39}$$

where q_e is the electron charge, k_B is the Boltzmann constant, T is the temperature, $\hbar$ is the reduced Planck constant, τ is the electron relaxation time, and μ_c is the chemical potential. Note that at the frequencies up to the visible range, $|\sigma_{\text{intra}}| >> |\sigma_{\text{inter}}|$, and therefore,

$$Z(\omega) \approx (Z_0\sigma_{\text{intra}})^{-1} = (1/\tau - i\omega)/(Z_0 C), \tag{40}$$

Natural plasmon modes of a graphene strip are usually viewed as the modes of the surface-wave Fabry–Perot resonator. Then, the empirical characteristic equation for such modes is

$$\sin\left(g_{plas}d + \eta\right) \approx 0, \tag{41}$$

where g_{plas} is the wave number (propagation constant) of the plasmon-guided wave of infinite sheet of graphene located on the interface between dielectric and air and η is the phase of the reflection coefficient of that wave from the strip edge (here, we assume that the absolute value of the reflection coefficient equals 1). According to [36], if $|Z^2| >> 1$, then the wave number of the plasmon-guided wave is

$$g_{plas}^2 \approx k^2(1+\varepsilon)\left[\frac{1}{2} - Z^2(1+\varepsilon)\right] + O\left(|Z|^{-2}\right). \tag{42}$$

and the best fit with the first-order plasmon mode is obtained when $\eta = \pi/4$.

Substituting (40) and (42) into (41) and neglecting the terms other than the leading one, we conclude that the natural frequencies of the plasmon modes P_m of the graphene strip are given by

$$f_m^P \approx \left[\frac{cZ_0 C(\pi m - \psi)}{d(1+\varepsilon)}\right]^{1/2}, m = 1, 2, \ldots, \tag{44}$$

As visible from (44), these frequencies are inverse-proportional to the square root of the strip width, d, and proportional to the mode index, m. They also scale as the square root of the graphene chemical potential. Therefore, one can manipulate them by changing the DC bias. The Q-factors of the plasmon modes are between 10 and 100 and depend mainly on the relaxation time, τ.

6.4 | Lattice modes of periodic open resonator

In addition to the dielectric-slab and graphene-strip modes, our metasurface possesses specific 'collective' modes that appear because of periodicity; these are the lattice modes (also called grating modes [28], L_{mn}. These mode resonances have been analysed for the PEC-strip-on-substrate grating in [23, 24] and the graphene-strip gratings inside a slab in [14, 21]. Here, the index m corresponds to the 'parent' RA (35) because their complex frequencies tend to the latter if the slab thickness shrinks to zero. Still, at any finite thickness, they are shifted in the main term by the frequency-dependent factor $g_n^H/k_0 > 1$,

$$f_{\pm mn}^{HL} \approx \frac{cmk_0\left(pg_n^H\right)^{-1}}{1 \pm \cos\alpha}, m = 1, 2, \ldots, n = 0, 1, 2, \ldots \tag{45}$$

Here, g_n^H is the wave number of the n-th guided wave TM_n of the bare dielectric slab [37]. Note that as the RA frequencies are purely real-valued, the lattice-mode Q-factors are controlled by the slab thickness—mainly, $Q_{mn}^{HL} = O(m^{-1}p^4/h^4)$—so that if the slab vanishes, all Q_{mn}^{HL} turn to infinity. However, it is known that the Poynting theorem prohibits purely real-valued frequencies of natural modes of open resonators [38]. Indeed, in the limit, the complex poles of lattice modes fall into the wolf-pits of RA branch points and thus vanish.

Today, it clear that the lattice-mode resonances are responsible for many remarkable phenomena explained earlier from different points of view. Among them, besides those mentioned in the introduction, there are the 'large phased-array scan blindness effect' [39–41], 'anomalous antenna Q-factors' [42], and 'guided-mode resonance' [43].

7 | NUMERICAL RESULTS: INTERPLAY OF RESONANCES

In the computations, we follow [14, 21] and assume the following graphene parameters: temperature $T = 300$K, chemical potential $\mu_c = 0.39$ eV, and electron relaxation $\tau = 1$ ps. The latter value is somewhat overoptimistic, as the best CVD-graphene samples available today have twice the smaller value of relaxation time; we have selected it to emphasize the plasmon resonances. At the end of this section, we address the tuneability of these resonances with the aid of the potential μ_c.

In Figure 4a, the plots of the reflectance (12) versus the frequency presented are in the range from 0 to 10 THz at the normal incidence of the H-polarized plane wave on a grating of graphene strips with a rather small filling factor, $d/p = 0.2$, in the free space and on a rather thin substrate with $h/p = 1/7$ and relative permittivity values 2.25 and 4.2.

The plots in Figure 4b show similar dependences of the absorbance for the same parameters. We do not show the plots for the transmittance because $P_{tr} = 1 - P_{ref} - P_{abs}$.

Note that the RA frequencies, which correspond to $\kappa = 1$ and 2, are found to be 4.286 THz and 8.571 THz, respectively. In addition, one can see several peaks and Fano-shaped double extremums of the reflectance and absorbance. They correspond to the natural modes of our metasurface denoted as in Section 3. The zoomed-up spectra on panels (b) and (c) show better resolution of the narrow ranges containing sharp peaks on the high-Q lattice modes L_{10} and L_{20}.

In addition, the spectra in Figure 4a,b reveal medium-Q resonances on the plasmon modes P_1, P_3, and P_5. At normal incidence, the plasmon modes with even indices remain 'dark modes'; they are not excited because their eigenfields are orthogonal in symmetry to the plane wave. Note that if $\varepsilon = 4.2$, the lattice mode L_{10} hybridizes with the plasmon mode P_3 around 4.03 THz.

The resonance on the principal plasmon mode P_1 dominates at the frequencies lower than the first RA. Its presence ruins the so-called Hertz effect of the good transparency, in the H-polarization regime, of gratings made of wires or strips that conduct well and are placed with periods smaller than the wavelength; note that the same takes place for the noble-metal gratings in the visible range [28]. However, enhanced reflection is accompanied by sizeable absorption.

Below 0.5 THz (this value depends on ε and μ_c), the on-substrate graphene-strip grating with$d = 14\ \mu$m wide strips displays rather good polarization discrimination in Hertz sense. The exact position of the principal plasmon resonance P_1 depends on the strip width in accord with (44), which opens up opportunities to design tuneable sub-THz polarizers.

Panels (b) and (c) demonstrate that if the optical contrast of the substrate and the host medium becomes smaller (the same happens if the substrate becomes thinner), then the lattice-mode peaks of high reflection and absorption move closer to the RA frequencies, and their Q-factors become larger. The distance from RA is mediated by the principal guided wave TM_0 of the dielectric slab in accord with (45).

Finally, we would like to draw the reader's attention to the wide bell-like resonances in Figure 4a, which are absent in Figure 4b, at 4.1 THz for $\varepsilon = 4.2$ and 5.0 THz for $\varepsilon = 2.25$. These are the slab-mode resonances. They do not show up in the absorbance because here, the slab is assumed lossless.

The identification presented above of the natural modes responsible for the resonances in THz wave scattering and absorption by the considered metasurface is supported by the near-field portraits presented in Figures 5 to 7. Namely, in Figure 5a,b one can see the standing waves along the grating formed by the ±1st Floquet harmonics and in Figure 5c,d by the ±2nd ones [14, 28]. In Figure 6, the plasmon-mode fields stick to the strips similarly to [16], while in Figure 7, the slab-mode fields, independent on x, are only slightly perturbed by the presence of the strips.

The next series of results demonstrates what happens to the frequency dependences of reflectance and absorbance if the angle of the plane wave incidence starts deviating from normal. Plots in Figure 8 correspond to the on-substrate grating with period $p = 70\ \mu$m made of narrow graphene strips with $d = 7\ \mu$m and those in Figure 9—to the grating of the same period made of wide strips with $d = 63\ \mu$m. Other parameters of the substrate and graphene are the same as in Figure 4.

If the strips are narrow (Figure 8), then for this combination of parameters at the normal incidence there is a broad slab-mode resonance S_1 at around 5 THz, on the red slope of which there is a principal plasmon-mode resonance P_1 at 3.855 THz and on the blue slope–the next P_3 mode resonance, which is much weaker. Double RA of the orders ±1 is at 4. 286 THz. Slightly red-shifted from this RA is the sharp lattice-mode resonance L_{10} and its higher-order sister L_{20} is seen at 7.746 THz. As soon as the angle of incidence departs from normal, double RA splits into two separate ones for the -1st and +1st Floquet harmonics.

Each of them is accompanied by the corresponding lattice-mode resonance on the red side. Note that the negative-index RA is accompanied by resonances on the L_{-mn} modes that remained 'dark' at the normal incidence because their field symmetry was orthogonal to the plane wave. Note that both plasmon-mode and slab-mode resonances remain intact so that off the lattice-mode frequencies, all curves overlap.

If the strips are wide (the grating is a sheet of graphene with narrow slots) as in Figure 9, then at the normal incidence, the slab-mode resonance is blue-shifted to 6 THz while the principal plasmon P_1 is red-shifted to 1 THz.

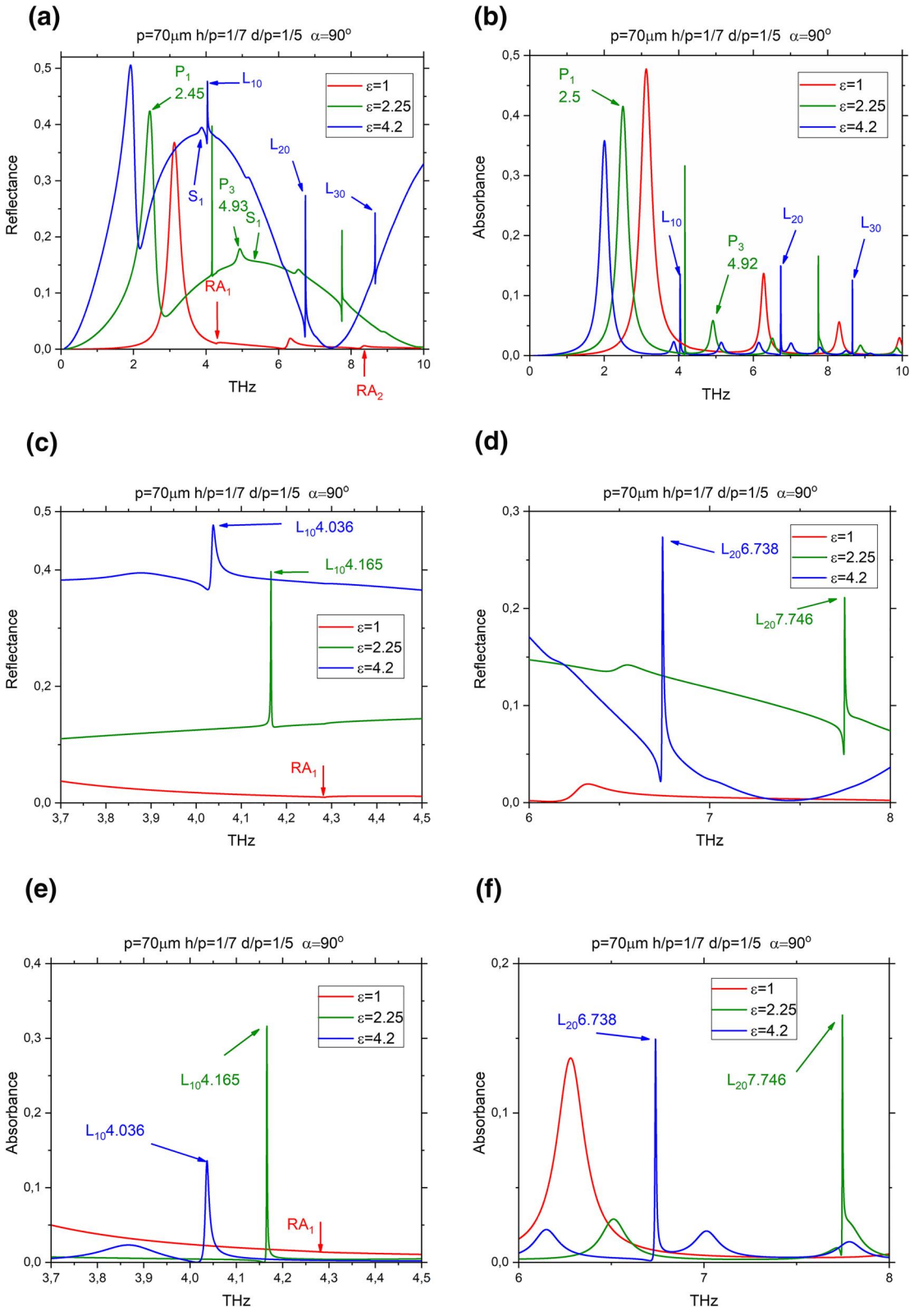

FIGURE 4 The reflectances (a), (c), (d) and absorbances (b), (e), (f) of the free-standing and on-substrate gratings with period $p = 70\ \mu$m, $d/p = 0.2$, and $h/p = 1/7$ versus the frequency for three values of the permittivity, $\varepsilon = 1$, 2.25, and 4.2 (a), and zooms of (a) and (b) near the L_{10} (c), (e) and the L_{20} (d), (f) mode resonances

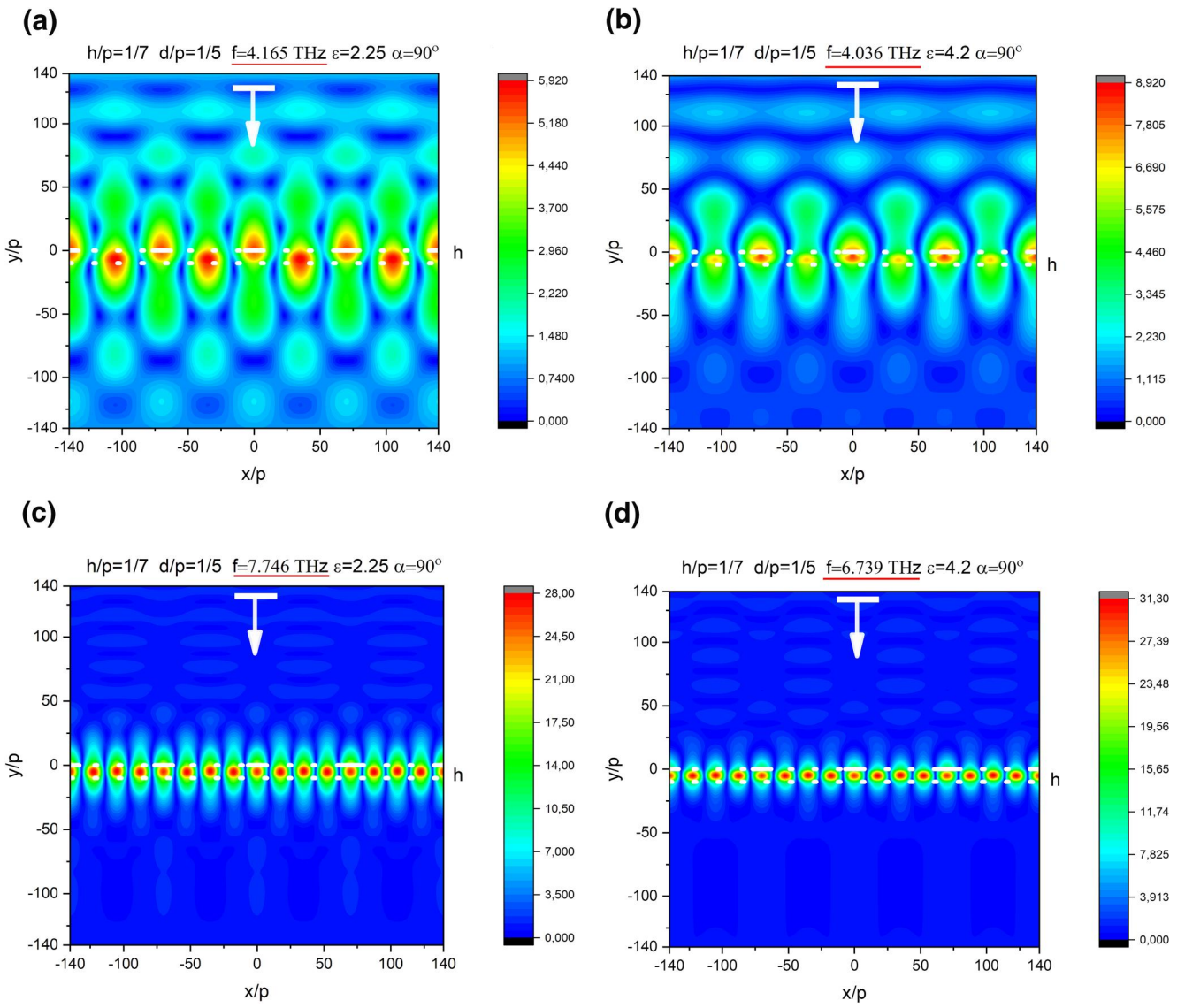

FIGURE 5 The magnetic field patterns for four periods in the resonances on the lattice modes L_{10} and L_{20} at the normal incidence for the same grating as in Figure 4 with $\varepsilon = 2.25$: (a) $f = 4.165$ THz (c) $f = 7.746$ THz; and with $\varepsilon = 4.2$: (b) $f = 4.036$ THz and (d) $f = 6.739$ THz

In this case, a departure of the angle of incidence from the normal entails the appearance of split resonances on the lattice modes $L_{\pm 10}$ and $L_{\pm 20}$, less intensive than on the narrow-strip grating. In addition, even-index plasmon modes P_2, P_4 etc. become visible, at least on the plots of absorbance.

As the DC tuneability of conductivity is graphene's most important characteristic for application features, we have computed the THz spectra of the reflectance, transmittance, and absorbance for various values of the chemical potential, μ_c. These dependencies are shown in Figure 10a,b,c.

As one can see, larger chemical potentials shift the plasmon-mode resonances to the blue and their peak values become somewhat smaller. This shift eventually yields, at $\mu_c = 1.5$ eV (see panel (d)), the situation where the real values of the complex natural frequencies of the medium-Q mode P_1 and the high-Q mode L_{10} coincide. In this situation, the broad peak of high (75%) reflection because of the plasmon mode becomes cut through by a narrower band of low (12%) reflection. In this band, the absorbance also drops to 0.1%, so that the transmittance exceeds 87%. Sometimes such an effect is called *electromagnetically induced transparency*. As a result of this effect, by varying the graphene chemical potential, one can change the transmittance/reflectance ratio of the H-polarized THz plane wave, which is the metasurface transparency, within a large dynamic range.

8 | CONCLUSIONS

In this work, we adapted the MAR technique based on the analytical solution of the RHP to the form suitable for accurate and efficient electromagnetic analysis of the metasurface made of graphene-strip grating on a dielectric substrate. The developed

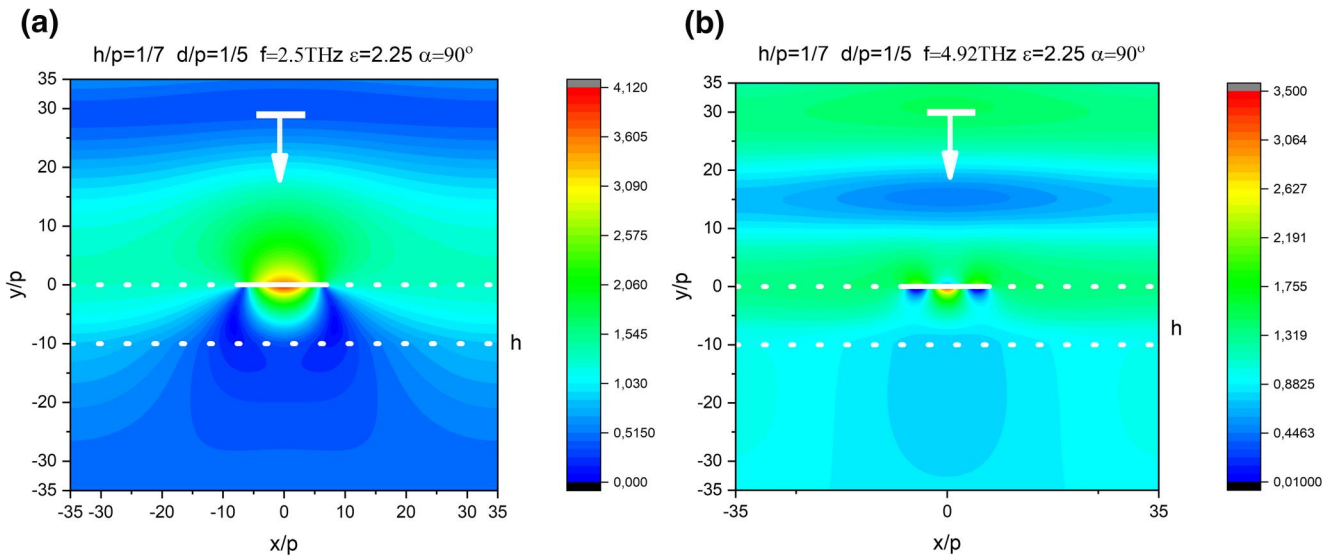

FIGURE 6 The magnetic field patterns for one period in the resonances on the plasmon modes P_1 and P_3 for the same grating as in Figure 4 with $\varepsilon = 2.25$: (a) $f = 2.5$ THz and (b) $f = 4.92$ THz

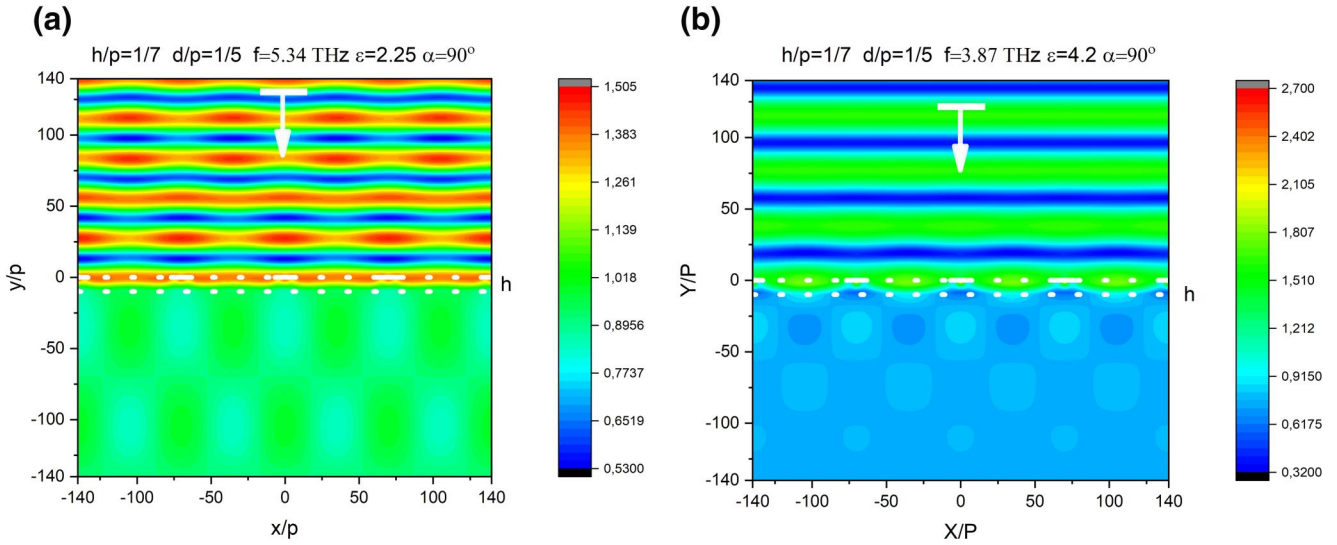

FIGURE 7 The magnetic field patterns for four periods in the resonances on the slab mode of substrate, S_1, for the same grating as in Figure 4 with (a) $\varepsilon = 2.25$ at $f = 5.34$ THz and (b) $\varepsilon = 4.2$ at $f = 3.87$ THz

numerical code is meshless, has a guaranteed convergence, and does not involve any numerical integrations. Using this fast and trusted numerical instrument, we have studied the interplay over the whole THz range of the resonances in plane wave scattering and absorption caused by three types of H-polarized natural modes. Two are well-known low-Q slab modes of the substrate and moderate-Q plasmon modes of the graphene strips. Besides those, the considered composite metasurface possesses ultra-high-Q lattice modes of various orders. The existence of these modes is the consequence of two factors: periodicity and presence of the substrate. This can be seen in the fact that their frequencies are tied to the RA frequencies but are shifted from them by the factors determined by the normalized wave numbers of the guided waves of the substrate. Lattice modes do not exist on a graphene-strip grating located in the free space but rather on such a grating supported by a thin substrate. Their Q-factors for infinite grating tend to infinity if the substrate becomes thinner; however, in the end, the corresponding complex poles disappear in the RAs, which are the branch points.

We have demonstrated that thanks to the tuneability of the plasmon modes with the aid of graphene's chemical potential, it is possible to realize DC bias-controlled electromagnetically induced transparency in the THz range on the metasurface of a microsized period. This can be useful in designing novel tuneable filters, modulators, and absorbers that use periodically patterned graphene.

It is worth emphasizing that accurate characterization of such fine resonance effects as those caused by the lattice

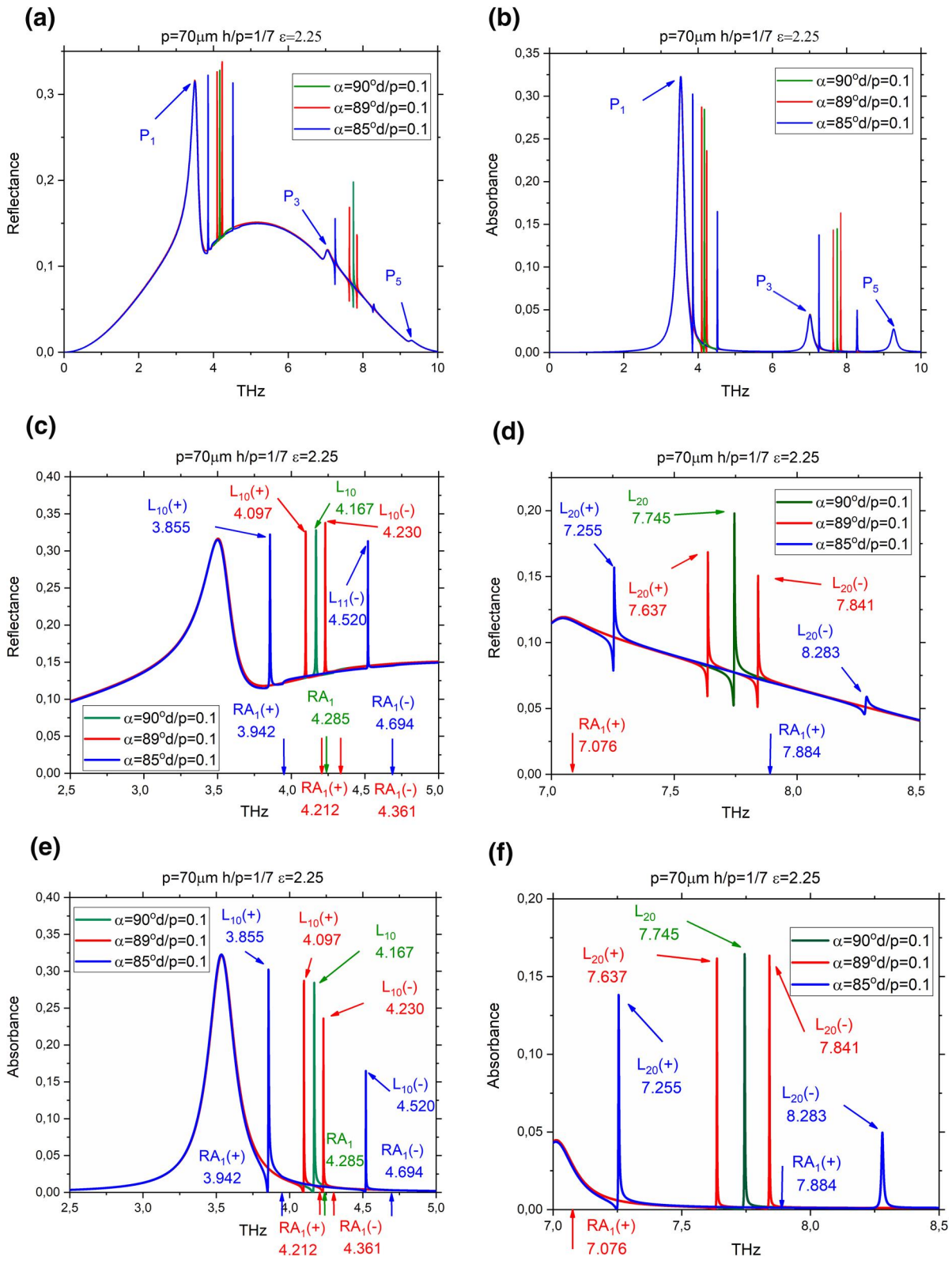

FIGURE 8 Inclined incidence on the on-substrate grating with narrow strips. The reflectance (a), (c), (d) and absorbance (b), (e), (f) for $p = 70\ \mu\text{m}$, $h/p = 1/7$, $\varepsilon = 2.25$, and $d/p = 0.1$ versus the frequency at three values of the angle of incidence, $\alpha = 90^\circ$, 89°, and 85°. The zooms near the lattice-mode resonances $L_{\pm 10}$ (b) and $L_{\pm 20}$ (c), are also shown

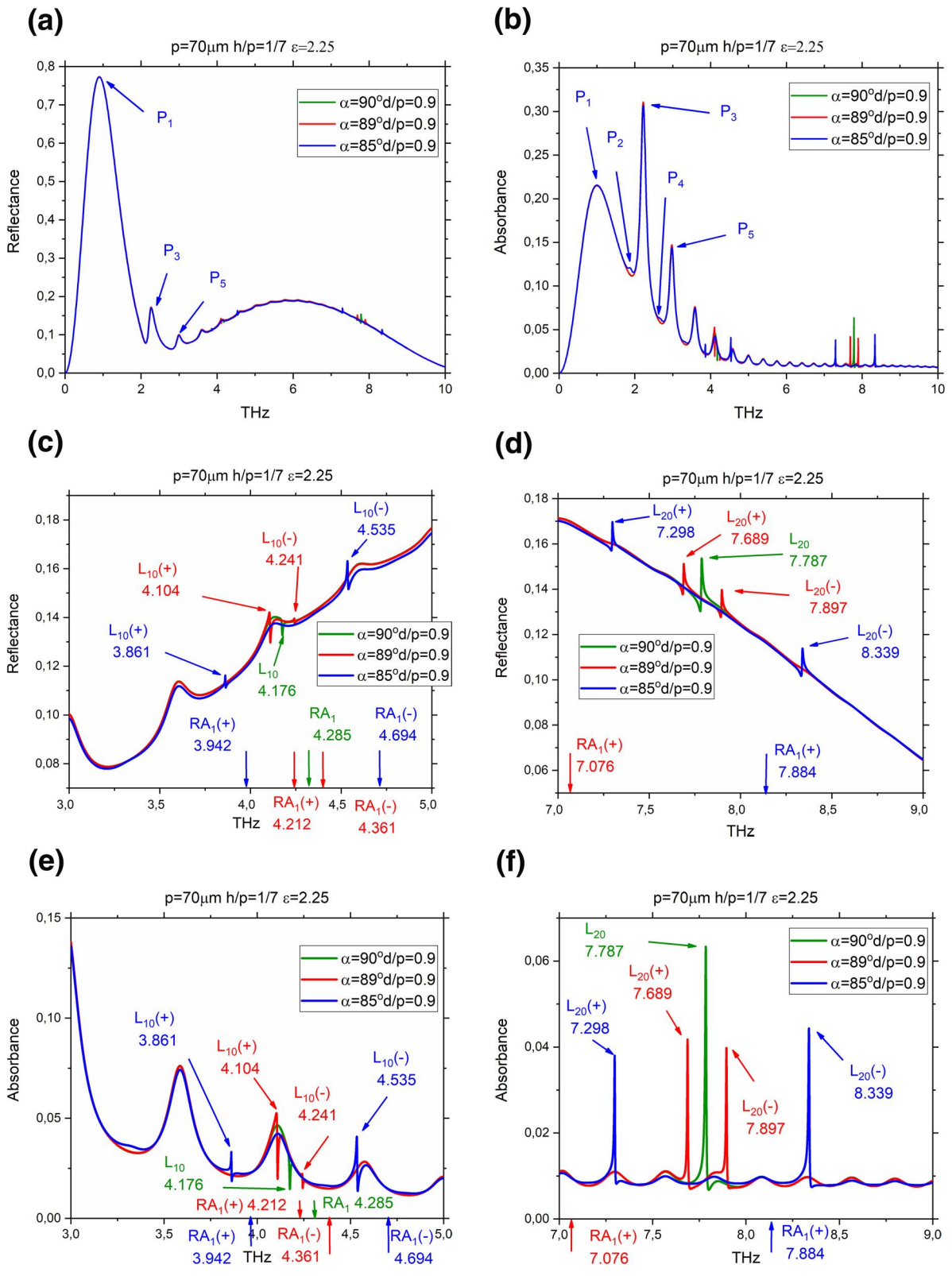

FIGURE 9 Inclined incidence on the on-substrate grating with narrow slots. The reflectance (a), (c), (d) and absorbance (b), (e), (f) versus the frequency at three angles of incidence for the same slab and grating parameters as in Figure 8 except for $d/p = 0.9$. The zooms near the lattice-mode resonances $L_{\pm 10}$ (c), (e) and $L_{\pm 20}$ (d), (f), are also shown

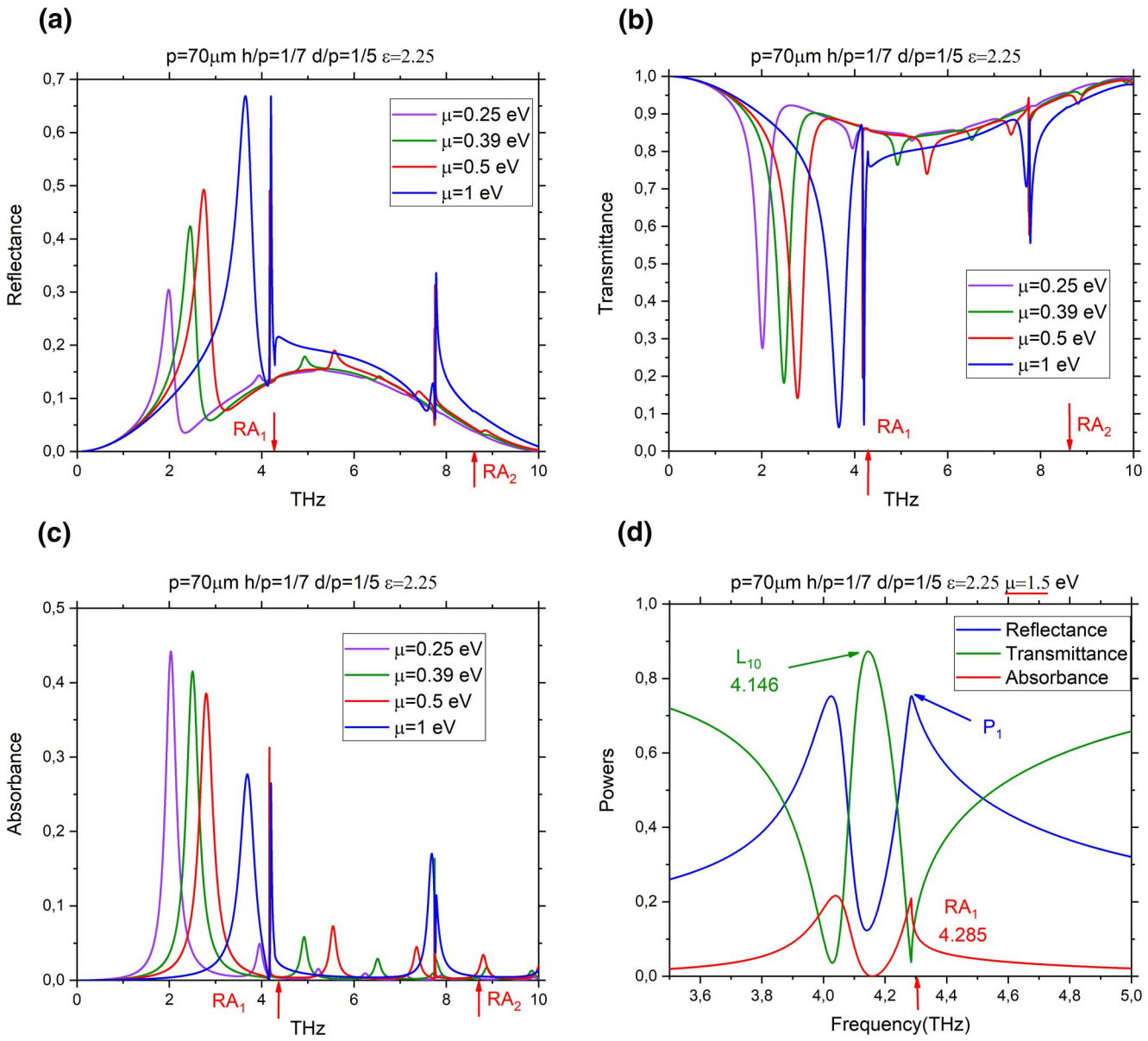

FIGURE 10 (a)–(c) Reflectance, transmittance, and absorbance versus the frequency of the H-polarized plane wave normally incident of the on-substrate narrow-strip grating with $p = 70\ \mu m$, $h/p = 1/7, d/p = 1/5$, and $\varepsilon = 2.25$ for the four values $\mu_c = 0.25$ eV, 0.39 eV, 0.5 , and 1 eV. (d) Zoom of the narrow band around P_1, L_{10}, and RA_1 frequencies at $\mu_c = 1.5$ eV

modes needs an adequate numerical technique. Indeed, even if a substrate is moderately thin, say, with a thickness of 1 μm, their Q-factors can reach 10^6 and thus, numerical solutions must deliver six or more correct digits. This is apparently beyond the capabilities of existing rough methods and commercial codes. In contrast, the presented technique can easily demonstrate such performance; thanks to very high efficiency, it can also be applied in numerical optimization software.

ACKNOWLEGEMENT

This work was supported, in part, by the National Research Foundation of Ukraine, project # 2020.02.0150.

ORCID

Fedir O. Yevtushenko https://orcid.org/0000-0003-3119-8315
Sergii V. Dukhopelnykov https://orcid.org/0000-0002-0639-988X

REFERENCES

1. García de Abajo, F.J.: Graphene plasmonics: challenges and opportunities. ACS Photonics. 1(3), 135–152 (2014)
2. Low, T., Avouris, P.: Graphene plasmonics for terahertz to mid-infrared applications. ACS Nano. 8(2), 1086–1101 (2014)
3. Rodrigo, D., et al.: Mid-infrared plasmonic biosensing with graphene. Science. 349(6244), 165–168 (2015)

4. Ullah, Z., et al.: A review on the development of tunable graphene nanoantennas for terahertz optoelectronic and plasmonic applications. Sensors. 20, (5), 1401 (2020)
5. Hanson, G.W.: Dyadic Green's functions and guided surface waves for a surface conductivity model of graphene. J. Appl. Phys. 103, 064302 (2008)
6. Shukla, S., Kang, S.Y., Saxena, S.: Synthesis and patterning of graphene: Strategies and prospects. Appl. Phys. Rev. 6(2), 021311 (2019)
7. Thongrattanasiri, S., Koppens, F.H.L., De Abajo, F.J.G.: Complete optical absorption in periodically patterned graphene. Phys. Rev. Lett. 108, 047401/5 (2012)
8. Vasic, B., Isic, G., Gajic, R.: Localized surface plasmon resonances in graphene ribbon arrays for sensing of dielectric environment at infrared frequencies. J. Appl. Phys. 113(1), 113110 (2013)
9. Fuscaldo, W., et al.: Efficient 2-D leaky-wave antenna configurations based on graphene metasurfaces. Int. J. Microw. Wireless Technol. 9(6), 1293–1303 (2017)
10. Rodrigo, D., et al.: Double-layer graphene for enhanced tunable infrared plasmonics. Light: Science Applicat. 6(6), e16277 (2017)
11. Xu, Z., et al.: Desingn of a tunable ultra-broadband terahertz absorber based on multiple layers of graphene ribbons. Nanoscale Res. Lett. 13(1), 143 (2018)
12. Hwang, R.-B.: A theoretical design of evanescent wave biosensors based on gate-controlled graphene surface plasmon resonance. Sci. Rep. 11, 1999 (2021)
13. Du, X., et al.: Approaching ballistic transport in suspended graphene. Nature Nanotech. 3, 491–495 (2008)
14. Zinenko, T.L., Matsushima, A., Nosich, A.I.: Surface-plasmon, grating-mode and slab-mode resonances in THz wave scattering by a graphene strip grating embedded into a dielectric slab. IEEE J. Sel. Top. Quant. Electron. 23(4), 4601809 (2017)
15. Čtyroký, J., et al.: Graphene on an optical waveguide: comparison of simulation approaches. Opt. Quant. Electron. 52(3), 149 (2020)
16. Shapoval, O.V., et al.: Integral equation analysis of plane wave scattering by coplanar graphene-strip gratings in the THz range. IEEE Trans. THz Sci. Technol. 3(5), 666–674 (2013)
17. Kaliberda, M.E., Lytvynenko, L.M., Pogarsky, S.A.: Modelling of graphene planar grating in the THz range by the method of singular integral equations. Frequenz. 72, 277–284 (2018)
18. Zinenko, T.L.: Scattering and absorption of terahertz waves by a free-standing infinite grating of graphene strips: analytical regularization analysis. J. Optics. 17(5), 055604/8 (2015)
19. Medina, F., Mesa, F., Skigin, D.C.: Extraordinary transmission through arrays of slits: a circuit theory model. IEEE Trans. Microwave Theory Techn. 58(1), 105–115 (2010)
20. Lucido, M.: An analytical technique to fast evaluate mutual coupling integrals in spectral domain analysis of multilayered coplanar coupled striplines. Microw Opt Technol Lett. 54(4), 1035–1039 (2012)
21. Zinenko, T.L., Matsushima, A., Nosich, A.I.: Terahertz range resonances of metasurface based on double grating of microsize graphene strips inside dielectric slab. Proc. Royal Society A. 476(2240), 20200173 (2020)
22. Tretyakov, O.A., Shestopalov, V.P.: Electromagnetic wave diffraction by a plane metal grating lying on a dielectric layer. Izv. VUZov Radiofizika. 6(2), 353–363 (1963)
23. Yevtushenko, F.O., Dukhopelnykov, S.V., Nosich, A.I.: H-polarized plane-wave scattering by a PEC strip grating on top of a dielectric substrate: Analytical regularization based on the Riemann-Hilbert Problem solution. J. Electromagn. Waves. Appl. 34(4), 483–499 (2020)
24. Yevtushenko, F.O., Dukhopelnykov, S.V., Zinenko, T.L.: E-polarized plane-wave scattering from a PEC strip grating on a dielectric substrate: Analytical regularization and lattice-mode resonances. J. Electromagn. Waves Applicat. 35(10) (2021) (#TEWA-2020-0623.R1)
25. Hessel, A., Oliner, A.A.: A new theory of Wood's Anomalies on optical gratings. Appl. Opt. 4(10), 1275–1297 (1965)
26. Lomakin, V., Michielssen, E.: Transmission of transient plane waves through perfect electrically conducting plates perforated by periodic arrays of subwavelength holes. IEEE Trans. Antennas Propagat. 54(3), 970–984 (2006)
27. Belotelov, V.I., et al.: Enhanced magneto-optical effects in magnetoplasmonic crystals. Nature Nanotech. 6, 370–376 (2011)
28. Byelobrov, V.O., et al.: Periodicity Matters: grating or lattice resonances in the scattering by sparse arrays of subwavelength strips and wires. IEEE Antennas Propag. Mag. 57(6), 34–45 (2015)
29. Babicheva, V.E, Evlyukhin, A.B.: Resonant lattice Kerker effect in metasurfaces with electric and magnetic optical responses. Laser Photon Rev. 11(6), 1700132 (2017)
30. Kravets, V.G., et al.: Plasmonic surface lattice resonances: a review of properties and applications. Chem Rev 118, 5912–5951 (2018)
31. Yachin, V.V., Zinenko, T.L., Mizrakhy, S.V.: Resonance enhancement of Faraday rotation in double-periodic gyromagnetic layers analysed by the method of integral functionals. J. Opt. Soc. Am. B. 35, 851–860 (2018)
32. Ivzhenko, L.I., et al.: Experimental observation of tunable wood type resonances in an all-ferrodielectric periodical metasurface. Opt. Lett. 45(19), 5514–5517 (2020)
33. Utyushev, A.D., Zakomirnyi, V.I., Rasskazov, I.L.: Collective lattice resonances: plasmonics and beyond. Reviews in Physics. 6, 100051 (2021)
34. Volakis, J.L., Lin, Y.C., Anastassiu, H.: TE characterization of resistive strip gratings on a dielectric slab using a single edge-mode expansion. IEEE Trans. Antennas Propagat. 42(2), 205–212 (1994)
35. Byelobrov, V.O., Nosich, A.I.: Mathematical analysis of the lasing eigenvalue problem for the optical modes in a layered dielectric cavity with a quantum well and distributed Bragg reflectors. Opt. Quant. Electron. 39(10-11), 927–937 (2007)
36. Dukhopelnykov, S.V., Sauleau, R., Nosich, A.I.: Integral equation analysis of terahertz backscattering from circular dielectric rod with partial graphene cover. IEEE J. Quant. Electron. 56(6), 8500208 (2020)
37. Tsitsas, N.L., Valagiannopoulos, C., Nosich, A.I.: Excitation of guided waves on a lossless dielectric slab by an E-polarized complex source point beam. IEEE Trans. Antennas Propagat. 67(8), 5532–5543 (2019)
38. Smotrova, E.I., et al.: Optical theorem helps understand thresholds of lasing in microcavities with active regions. IEEE J. Quantum Electron. 47(1), 20–30 (2011)
39. Oliner, A.A.: On blindness in large phased arrays. Alta Freq. 38, 221–228 (1969) Special Issue
40. Pozar, D., Schaubert, D.: Scan blindness in infinite phased arrays of printed dipoles. IEEE Trans. Antennas Propagat. 32(6), 602–610 (1984)
41. Koo, H., Nam, S.: Mechanism and elimination of scan blindness in a T-printed dipole array. IEEE Trans. Antennas Propagat. 68(1), 242–253 (2020)
42. Ludvig-Osipov, A., Jonsson, B.L.G.: Stored energies and Q-factor of two-dimensionally periodic antenna arrays. IEEE Trans. Antennas Propagat. 68(8), 5989–6002 (2020)
43. Inoue, J., et al.: Design of a narrowband retroreflector based on guided-mode resonance. J. Opt. Soc. Am. A. 37(4), 579–583 (2020)

How to cite this article: Yevtushenko, F.O., et al.: Electromagnetic characterization of tuneable graphene-strips-on-substrate metasurface over entire THz range: analytical regularization and natural-mode resonance interplay. IET Microw. Antennas Propag. 15(10), 1225–1239 (2021). https://doi.org/10.1049/mia2.12158